#### **PAPER**

Nondestructive ultrasonic evaluation of fused deposition modeling based additively manufactured 3D-printed structures

To cite this article: Yuqi Jin et al 2020 Smart Mater. Struct. 29 045020

View the <u>article online</u> for updates and enhancements.

Smart Mater. Struct. 29 (2020) 045020 (8pp)

https://doi.org/10.1088/1361-665X/ab74b9

# Nondestructive ultrasonic evaluation of fused deposition modeling based additively manufactured 3D-printed structures

Yuqi Jin<sup>1,2</sup>, Ezekiel Walker<sup>3</sup>, Hyeonu Heo<sup>1</sup>, Arkadii Krokhin<sup>1</sup>, Tae-Youl Choi<sup>2,4</sup> and Arup Neogi<sup>1,4</sup>

E-mail: arup@unt.edu

Received 19 September 2019, revised 15 January 2020 Accepted for publication 10 February 2020 Published 9 March 2020



#### **Abstract**

The quality control of 3D printed structures is significant for the reliability of additively manufactured objects. A novel remote sensing technique for characterizing 3D printed structures was developed by non-destructive ultrasonic imaging of a commonly used thermoplastic object such as acrylonitrile butadiene syrene (ABS). The quality of the additively manufactured ABS slab printed by fused deposition modeling (FDM) technique was evaluated by imaging effective density technique. The infill density of the FDM printed structures were modified by varying the motor speed of the printing extruder. An ultrasonic raster scan of the 3D printed structure using the novel effective density imaging technique distinguished the contrast in density with a very high resolution in the density variation. In addition to the lateral scanning, the density characterization was also effective when applied axially and can probe deep inside the additively manufactured object. The experimentally measured density variation agrees well with the theoretically calculated density values as a function of flow rate. The combined lateral and axial capabilities of the imaging technique make it a promising diagnostic tool for an *in situ* inspection method of optimizing FDM printing and quality control of 3D printed objects.

Keywords: FDM printing, ultrasonic imaging, nondestructive testing, effective density

1

(Some figures may appear in colour only in the online journal)

#### 1. Introduction

Additive manufacturing has been broadly used for fabricating highly customizable designs and realizing complex geometric in various applications such as biomedicine, mechanical designs, and fundamental research. Although 3D printing technology provides flexibility in the design to manufacture the shape any object, the mechanical properties are rather non-uniform and significantly inferior compared to conventionally manufactured objects. Fused deposition modeling (FDM) is the most common 3D printing method on the

market due to its relatively low cost and fast printing speed. Various thermoplastics such as Nylon, Acrylonitrile Butadiene Styrene (ABS), Polylactic Acid (PLA), and carbon fiber composites material [1] can be used in FDM printers. The thermoplastic filament is usually heated to temperatures between the glass transition and melting temperature of the material to reshape it into a designed arrangement and build the desired geometry. Recently FDM printers have been used for novel applications such as house construction [2], fluidic devices [3] and microwave antennas [4, 5]. Those recently invented new applications usually use 100% infilled printing

<sup>&</sup>lt;sup>1</sup> Department of Physics, University of North Texas, PO Box 311427, Denton, TX 76203, United States of America

<sup>&</sup>lt;sup>2</sup> Department of Mechanical and Energy Engineering, University of North Texas, 3940 North Elm Suite F101, Denton, TX 76207, United States of America

<sup>&</sup>lt;sup>3</sup> Echonovus Inc., 1800 South Loop 288 STE 396 #234, Denton, TX 76205, United States of America

<sup>&</sup>lt;sup>4</sup>Center for Agile and Adaptive Additive Manufacturing, University of North Texas, Denton, TX 76207, United States of America

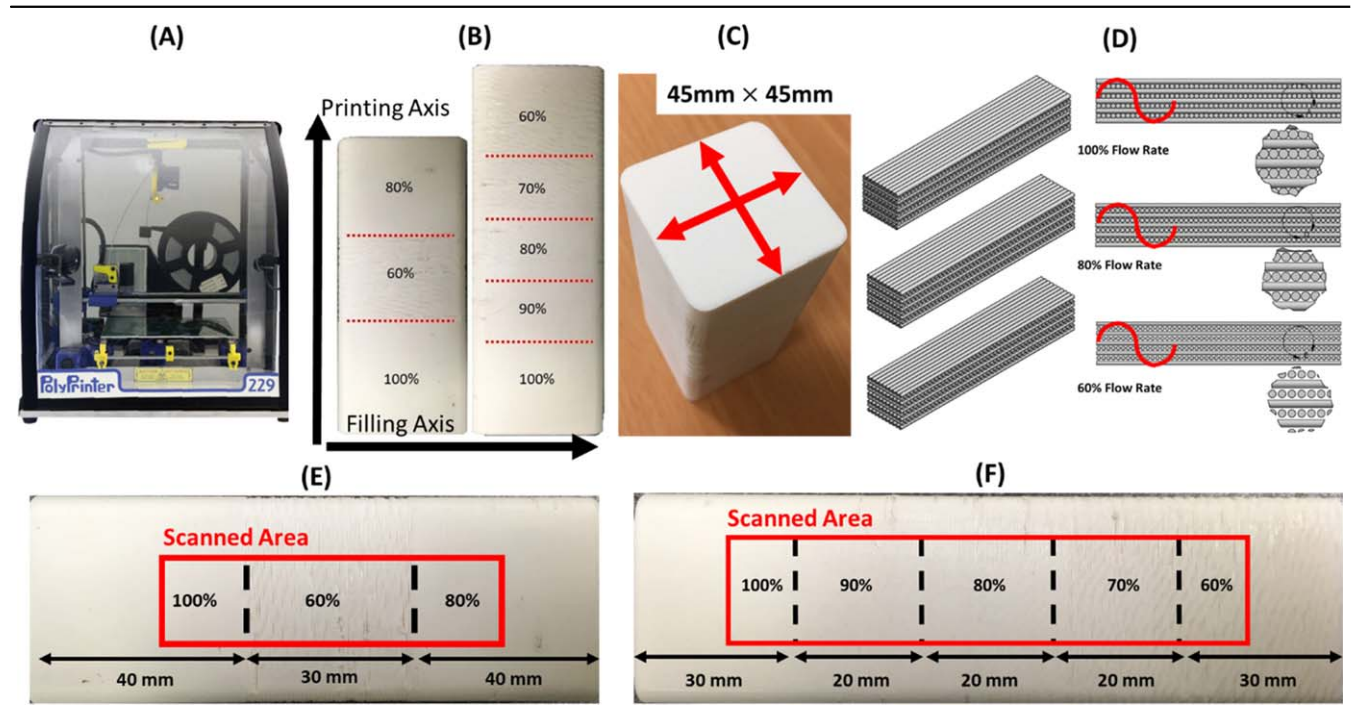


**Figure 1.** (A) Photograph of PolyPrinter 229 (from polyprinter.com), a single extruder FDM printer. (B) Photographs of printed sample. The operating condition of the printer was 100%, 60% and 80% flow rate in high density contrast sample, and 100%–60% with 10% flow rate interval in low density contrast sample. (C) Photograph of the sample illustrated the cross-section dimensions. Both samples have the same cross-section size and design. (D) CAD drawing for demonstrating effective nozzle diameter by decreasing flow rate. The estimated inside porosity should be small enough comparing with operating frequency of the ultrasound. The red Sine wave indicated averaged wavelength (around 4.5 mm) was much larger than the inside structure and porosity of the printed objects. (E) Photograph of the high density-contrast sample illustrated the dimensions on side view.

parameter for their purposes which were different from many conventional applications of FDM printing. Solid products are usually manufactured using 100% infilled printing setting of the FDM printer (figure 1). In G-code generator (slice software), the interior structure of the object is mapped normally in the octagonal format for infill settings that is not 100% (figure 1(c); lower right). For the 100% setting, the bulk of the object is filled by straight lines that are mapped with a resolution limited by the diameter of the nozzle. The 100% infilled solid structures are less porous in 3D printed structures and is more suitable for confining or avoiding fluids. It could also provide controllable and homogeneous dielectric properties in 3D printed substrates. Moreover, due to the wear and tear of the 3D printer components such as extruder nozzle, heater and extruding gear, etc, the density of actual products can also vary under the same software parameters setting. Unexpected voids might exist in the actual products manufactured by the same printer under differing material fabrication conditions. These small voids can be randomly distributed within the bulk of the 3D structures of various shapes and sizes and degrades the mechanical strength of the printed materials and structures.

The existing inspection test method for 3D printed products could be generally categorized in two types, mechanical tests and electromagnetic wave tests. The mechanical tests provide information in term of elasticity such as Young' modulus [6–9] and Shear modulus[10, 11], and plasticity such as strength [12, 13] and hardness [14]. The quality of 3D

printed objects defined as the amount of difference between real tested mechanical property values and desired values [15]. No existing mechanical testing technique determines density distribution on the 3D printed structures. In electromagnetic wave tests techniques, density of the printed structure is one of the main factor of quality inspection. The local porous volume fraction inside printed objects detected by x-ray [16] or gamma-ray [17]. For the demand of inspecting porosity in filament, a recent 3D magnetic field scan technique showed well performance [18]. Both mechanical tests and electromagnetic wave tests are broadly applied in research, but the critical limitation of those tests is the method are all destructive method either during testing or sample preparation. In this study, a novel non-destructive acoustic test method was applied on 3D printed structures to provide quantified evaluation in terms of effective density.

Ultrasonic techniques provide a non-destructive means of testing the elastic properties of solid structures that uses the longitudinal and transverse speed of sound in the material [19] and is useful for studying the variation in manufacturing processes [20] biomedical imaging [21] and characterization of materials properties of a bulk and surface structures. Ultrasonic characterization can provide the information about any change in certain physical properties such as elasticity and strength of the material from the longitudinal and transverse speed of sound in the medium [22]. Compared to conventional mechanical testing methods, such as tensile strength test, ultrasonic elasticity characterization does not

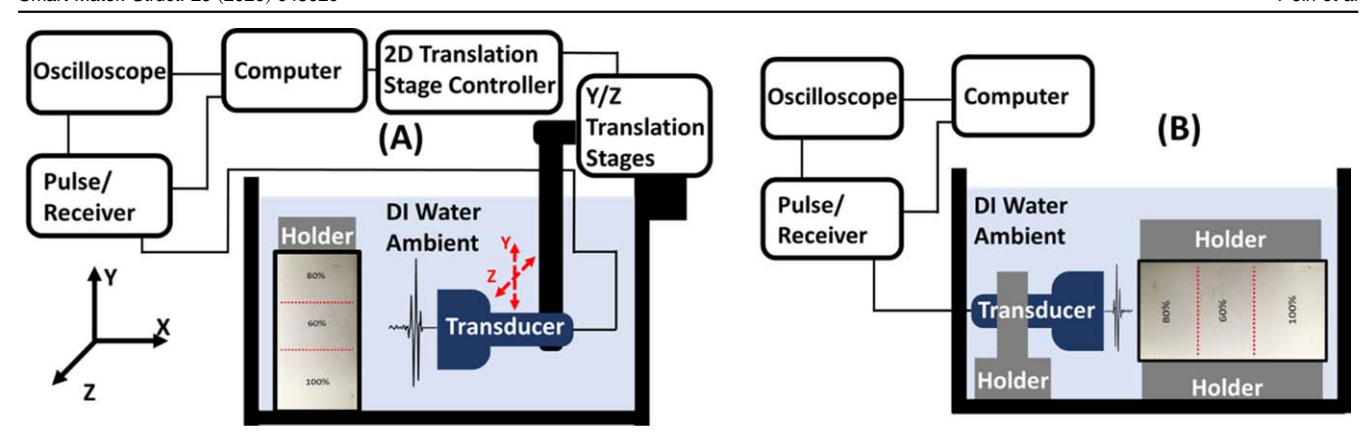


Figure 2. (A) Experimental setup of raster scanning effective density imaging in lateral plane. (B) Experimental setup of effective density characterization versus depth on axial direction.

require sample preparation and is less time consuming. Conventional ultrasonic imaging provides images in terms of either reflection intensity (A-mode) [23] or reflection time of flight (B-mode) [24]. By relating the ultrasound waves with the external stress, images can be represented in terms of elastic parameters such as Young's modulus [25] or shear modulus [26]. The techniques that combine applied stress deformation with ultrasound fall is categorized as ultrasound elastography (M-mode). However, the existing M mode imaging methods have limited application to industrial materials, such as metals and plastics, due to the large scanning volume or as the linear elastic deformation is normally too small to be detected by ultrasound.

In this study the quality of an FDM printed ABS object was investigated using a recently developed ultrasonic effective density imaging modality to detect small internal voids generated during the 3D printing process [27]. The density of the 3D-printed product would be less homogeneous compared to an ideal 3D printed structure using a 100% infilling setting due to unexpected void formation in ABS printed objects. Instead of determining the amount and size of each void inside of objects by x-ray in the microscopic scale [28], the effective density imaging technique provided the density information in bulk scale. The total local volume fraction of the void was obtained from the examined effective density values.

#### 2. Materials and methods

#### 2.1. Effective density imaging setup

An Olympus Panametrics V301 1" diameter 0.5 MHz immersion transducer was used to generate a pulse for the raster scan of samples and record signals reflected by the samples. The pulse source and time trigger were controlled internally by a JSR Ultrasonics DPR 300 Pulse/Receiver and the data was recorded by a Tektronix MDO 3024b. A Newport UE41PP translation stage controlled by a Universal Motion Controller/Driver Model ESP 300 was used to move the sample in a 2D plane (figure 2). Motion tagged data was acquired using an automated MATLAB® script.

The water level was high enough to fully cover the transducer and the sample in experiments. The image area of the high density-contrast sample was 5 mm at 2.5 mm interval along the filling axis (filling axis) by 60 mm with 2.5 mm interval (printing axis showed in figure 1). The image area of the low density-contrast sample was 6 mm with 1 mm interval (the filling axis illustrated in figure 2) by 80 mm with 1 mm interval (along the printing axis). The scanning rate was 51.2 signals per second. The transducer surface was aligned parallel to the rectangle surface as shown in figure 2 (left). The transducer surface was aligned parallel to the square surface as shown in figure 1(right).

## 2.2. Sample fabrication and estimated density theory

Various factors affect the quality and the bulk physical properties of the 3D printed structure even with a setting of 100% infill fraction. The average density of the 3D printed material is compared to a solid and homogenous structure prepared from a mold. An analytical model was developed that incorporated various print parameters to quantify the correlation amongst the effective density of a printed sample, the radius of the extruding filament, and an effective flow rate for the extruding thermoplastic. Figure 1 illustrates the printer, filling axes, and printing axis.

The extruder speed,  $v_{ex}$ , is defined as the speed of which filament of a fixed diameter is extruded,  $v_{ex} = \alpha v_0$ , where  $\alpha$  is the flow rate parameter,  $\alpha \in [0, 1]$ , and  $v_0$  is the maximum extrusion speed. The slice software has default assumption of a rectangular cross section of beads, because the layer thickness value in the software setting is usually smaller than the nozzle size. In this case, the compression effect on extruded filament makes the cross section be a rectangular shape with a rounded corner. In this study, the setting in the slice software still assumes rectangular shape beads. However, due to the fact that the infill layer thickness is comparable to the nozzle size, very limited compression stress is applied on the extruded filament during printing, which makes the beads much closer to a cylindrical shape instead of rectangular [29]. Our density calculation is thus based on cylindrical cross section of the beads.

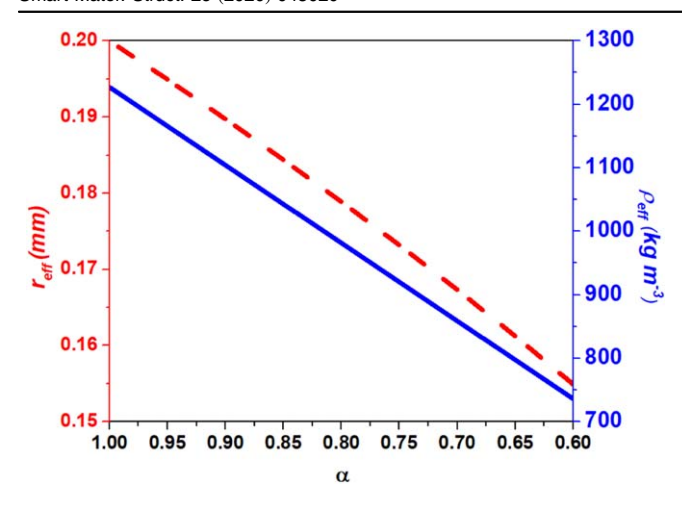


**Figure 3.** The red dash line showed the relationship between the percentage of flow rate and the effective nozzle diameter as  $r_{noz, eff} = (r_{noz}^2 \alpha v_0 / v_{X,Y,Z})^{1/2}$  described. The blue solid line illustrated the effective (estimated) density of each percentage of flow rate,  $\alpha$ , following  $\rho_{eff} = \rho_{ABS} r_{noz}$ ,  $eff^2 r_{noz}^{-2}$ .

The volume flow rate of extrusion is a function of  $v_{ex}$  and defined as  $\dot{V}_{ex} = \pi r_{noz}^2 v_{ex}$ , where  $r_{noz}$  is the radius of the extruder nozzle. The other parameters of the nozzle size, the extruder temperature, temperature of the heated deposit plate temperature, and the translational speed of the extruder are fixed as constants, Though the volume flow rate is a function of only the  $v_{ex}$  and  $r_{noz}$ , the translational speed of the stage affects the amount of material deposited per volume. Here, an effective extruder radius is defined to account for the translational speed,  $r_{noz,eff} = \sqrt{\frac{r_{noz}^2 \alpha v_0}{v_T}}$ , where  $v_T$  is the translational speed of the nozzle in the filling plane. From figure 3, it can be seen that the effective density,  $\rho_{eff}$ , and effective extruder radius are both linear functions of  $\alpha$ .

PolyPrinter 229 single filament extruder FDM printer (figure 2 left) was used to fabricate the ABS (Acrylonitrile Butadiene Styrene) sample with eSUN ABS filament. The 3D model slice software was KISSlicer64. The extruder temperature was set at 240 °C and the heated printing plate substrate to 110 °C. Two samples were both printed under the 100% in-fill condition and  $v_T = v_0 = 300 \text{ mm min}^{-1}$ . For ABS thermoplastic with  $v_0 = 300 \frac{\text{mm}}{\text{min}}$ , at  $\alpha = 1$ ,  $\rho_{eff}$  approaches the filament density of  $\rho_{ABS} = 1227 \frac{\text{kg}}{\text{m}^3}$  and  $\rho_{eff}$  can be expressed as  $\rho_{eff} = \rho_{ABS} r_{noz,eff}^2 r_{noz}^{-2}$  (figure 3) which is used to calculate estimated density comparing with experimental effective density in results section.

For this work, both a high and low contrast sample were fabricated and examined. The high contrast sample (HC) consisted of three regions with highly contrasting  $\alpha$  values of 1, 0.6, and 0.8. The dimensions of each section were 40, 30, and 40 mm. Additionally, a low contrast sample (LC) comprised of a gradient print of five  $\alpha$  values of 1.0–0.6 in intervals of 0.1 was printed under the same conditions. The dimensions of each section were 30, 20, 20, 20, and

30 mm. The total sample dimensions were 45 mm by 45 mm square cross-section with 100 mm height (HC) and 120 mm height (LC).

#### 3. Imaging theory

Effective density in raster scanned imaging was calculated as [27]

$$\rho = c^{-1} Z_0 \left( \frac{-1 - \frac{p_1}{p_e - p_0} - \sqrt{4 \frac{p_1}{p_e - p_0} + 1}}{\frac{p_1}{p_e - p_0} - 2} \right), \quad \frac{Z}{Z_0} > 1,$$

$$\rho = c^{-1} Z_0 \left( \frac{\left(1 - \frac{p_1}{p_e - p_0}\right) + \sqrt{1 - 4\frac{p_1}{p_e - p_0}}}{\frac{p_1}{p_e - p_0} + 2} \right), \ \frac{1}{3} \leqslant \frac{Z_1}{Z_0} < 1.$$

$$\tag{1}$$

where  $p_e$ ,  $p_0$ , and  $p_1$  are the maximum absolute amplitude values of the emitted pulse from the transducer, the first reflection from the front interface between water ambient and the sample, and the echo from the back interface between the sample and water ambient, respectively.  $p_a$  is calibrated from a separate bistatic experiment without a sample in the ambient medium.  $p_0$  and  $p_1$  are obtained from raster scan imaging. c is the local speed of sound derived from the time of flight in the sample at the scanned location, expressed as  $c = 2d/(time_{i,1} - time_{i,0})$ , where  $time_{i,1}$  and time<sub>i,0</sub>, are the start time of the first and second echo found by MATLAB<sup>®</sup> algorithm. d is the thickness of the sample. Effective density  $\rho$  is calculated from  $\rho = Z/c$ , where Z is the acoustic impedance of the sample at the scanned location. The reference acoustic impedance value of DI water ambient is  $Z_0 = \rho_0 c_0$ , where  $\rho_0 = 1000 \text{ kg m}^{-3}$  and  $c_0 = 1480 \text{ m s}^{-1}$  at room temperature.

Effective density characterization values are calculated as [27]:

$$p_{k} = \frac{Z_{n}}{Z_{0}} (p_{e} - \operatorname{sig}(Z_{1} - Z_{0}) | p_{0} |) \cdot \left( \prod_{i=2}^{k} t_{i-1,i} \right) \times r_{k-1,k} \left( \prod_{i=1}^{k} t_{i,i-1} \right), k = 1, 2, \dots, n,$$
 (2)

where the transmission and the reflection coefficients are  $t_{i-1,i}=(2Z_n)/(Z_{n-1}+Z_n)$  and  $r_{k-1,k}=(Z_n-Z_{n-1})/(Z_n+Z_{n-1})$  the reflection coefficient at the interface between layer (n-1) and n. The reflection coefficient of the interface between the last layer and ambient material is expressed as  $r_{k-1,0}=(Z_0-Z_{n-1})/(Z_{n-1}+Z_0)$ . n numbers of  $Z_n$  values are obtained by solving n numbers of equation (2) for the n numbers of layers in the samples. The effective density values are expressed as  $\rho_n=Z_nc_n^{-1}$ .

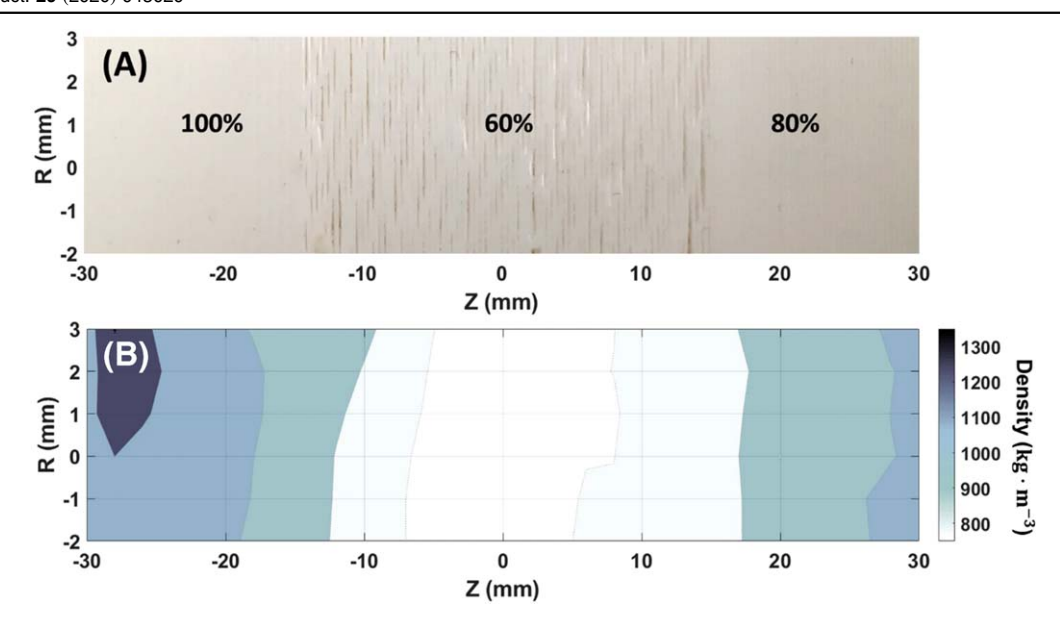


**Figure 4.** (A) Photograph of high density contrast sample with scale of scanned area. (B) Effective density imaging from equation (1). The color map was in the range between 750 and 1350 kg m $^{-3}$ . The dish line circled small area in middle had effective density values within 700 and 750 kg m $^{-3}$  which was outside of setted color map range.

# 4. Results and discussion

#### 4.1. Experiment 1 raster scan imagines

In high density-contrast sample scan, the total area in the raster scan was 60 mm in the vertical printing direction Z-axis at 2 mm intervals, and 6 mm in horizontal filling direction R-axis at  $2.5 \, \text{mm}$  intervals. As shown in figure 4(A), the width of the 100% and 80% sections were around 16 mm located on the two opposite sides of the sample. The middle zone was  $\sim$ 28 mm wide, having a theoretical effective density  $\sim$ 60% of the density of ABS filament. Besides the density of the regions, from figure 4(A), the porosity of the 60% region is visibly more extensive than either of the higher density zones. The effective density mapping is shown in figure 4(B) where the width of the 80% region measures  $\sim$ 14 mm and the 100% region  $\sim$ 16 mm respectively. The gradient pattern around each the regions was not negligibly small due to a large raster scan interval. The determined effective density of each region was about 1223.8  $\pm$  52 kg m<sup>-3</sup> (100%), 1017.4  $\pm$ 38 kg m<sup>-3</sup> (80%), and 751.8  $\pm$  43 kg m<sup>-3</sup> (60%).

In the low effective density contrast sample scan, 80 mm by 6 mm (Z by R) in 1 mm intervals along both axes was scanned. The width of the 100% and 60% zones were both around 10 mm wide, and the 90%, 80%, and 70% zones 20 mm (figure 5(A)). From 100% to 60% along Z-axis, the low contrast sample has a visible gradient of increasing surface roughness. The effective density image characterizes the gradient of the sample quite well, clearly distinguishing a decreasing density (figure 5(B)). The estimated width of each zone was about 13.0 mm (100%), 17.0 mm (90%), 22.0 mm (80%), 19.5 mm (70%), and 8.5 mm (60%). The averaged estimated effective density of the regions was  $1247.8 \pm 33$  kg m<sup>-3</sup> (100%),  $1131.8 \pm 19$  kg m<sup>-3</sup> (90%),  $1005.1 \pm 24$  kg m<sup>-3</sup> (80%),  $945.6 \pm 29$  kg m<sup>-3</sup> (70%), and  $655.8 \pm 32$  kg m<sup>-3</sup> (60%). The contrast between layers strongly

characterizes the transition in density between one layer to the next and aligns well with the known thickness of each layer.

Figures 4 and 5 provided clear illustrations of the effective density imaging comparing with photographs. However, the location of the interfaces between the regions were not clear by just presenting the contour figures. Hence, the exact location of the interfaces between the different regions were able to estimate by observing the contrast  $d\rho/dZ$  of effective density by distance. The location of the interface can be determined by the middle of (red shadowed zones) sharp change in  $d\rho/dZ$ . Figure 6 demonstrate the algorithm used to identify the interface location by a single row of effective density data from the imaging contour matrixes (figures 4(B) and 5(B)). As figure 6 (left) illustrated, the location of the left interface was accurately observed with 1 mm error in experiment 1. The interface between 80% and 60% regions had about 2.5 mm offset. Figure 6 (right) showed the interface locations of low contrast sample in experiment 2. The interface between 90% and 80% had about 1 mm offset. The interface 1 (between 100% and 90%) and interface 4 (between 70% and 60%) had about 2.5 mm errors. And the interface between 80% and 70% was precisely located at 10 mm on Z axis. From the results presenting by figure 6, the maximum error in interface location was about 2.5 mm which is about 1/10 of the operating transducer diameter (1 inch). Because the large diameter of transducers surface. The size of the transition region is a function of the size of the transducer and beam waist width. The 1" transducer used for the study has a full width half max about roughly 15 mm, so the resolution of the interface will be relatively low in effective density values. To further improving the resolution of effective density imaging, a smaller surface area transducer (such as penducer) can be used.

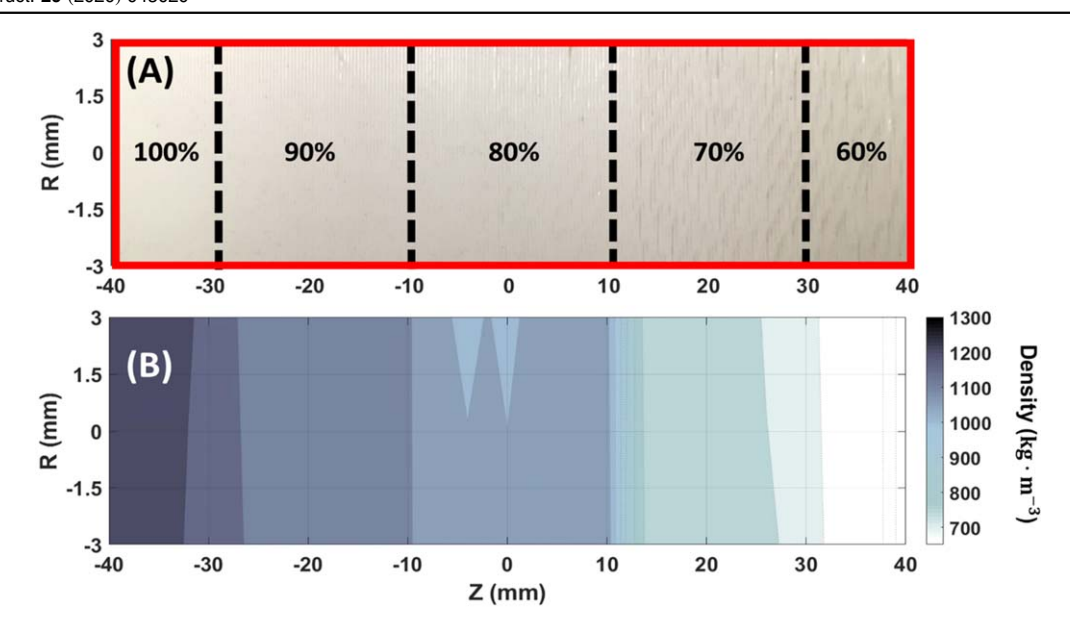


**Figure 5.** (A) Photograph of low density contrast sample with scale of scanned area. (B) Effective density imaging from equation (1). The color map was in the range between 650 and 1300 kg m $^{-3}$ . The dish line circled white small area had effective density values within 600 and 650 kg m $^{-3}$  which was outside of setted color map range.

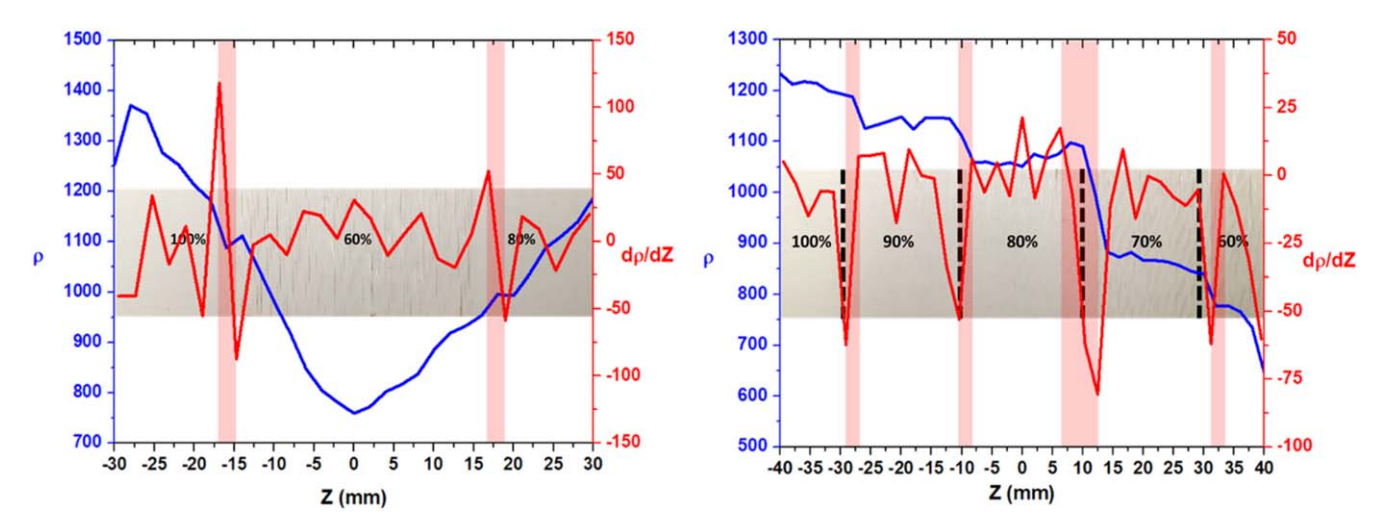


**Figure 6.** Blue solid line shows a row of effective density values from imaging contour. Red is its contrast which is expressed as  $d\rho/dZ$ , where the Z is the lateral distance in mm. (Left) experiment 1 high contrast sample imaging. (Right) experiment 2 low contrast sample imaging.

# 4.2. Experiment 2 axial scan along depth (density characterization)

In high effective density contrast sample, the interface between the regions provided high enough acoustic impedance mismatch to produce reflection at the interface in order to calculate the effective density values using equation (2) (figure 7). The characterization was performed in two directions  $0^{\circ}$  with the 100% region the incident surface, and  $180^{\circ}$ , where the 80% region serves as the incident material. The averaged characterized effective density values in  $0^{\circ}$  direction were  $1274.2\pm\ 27\ kg\ m^{-3}\ (100\%)$ ,  $1036.6\pm\ 42\ kg\ m^{-3}\ (80\%)$ , and  $816.5\pm\ 49\ kg\ m^{-3}\ (60\%)$ , and  $1243.8\pm\ 36\ kg\ m^{-3}\ (100\%)$ ,  $1084.9\pm\ 38\ kg\ m^{-3}\ (80\%)$ , and  $780.4\pm\ 32\ kg\ m^{-3}\ (60\%)$  in the  $180^{\circ}$  direction.

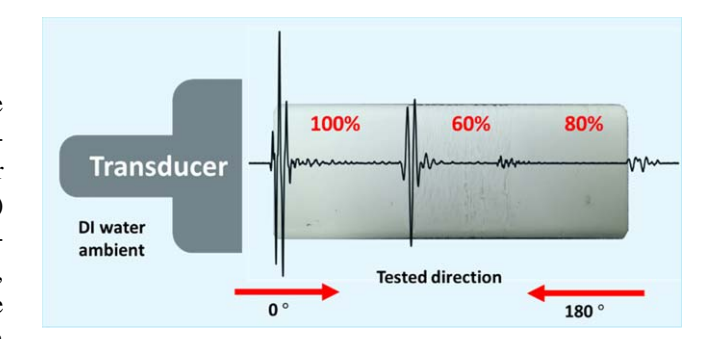


**Figure 7.** Schematic showing the overlap of the experimentally measured echos of the reflected signal at the four interfaces of the underlying optical image of the sample in water. Waveform from the direction of the emitter along the acoustical axis is considered to be the  $0^{\circ}$  direction.

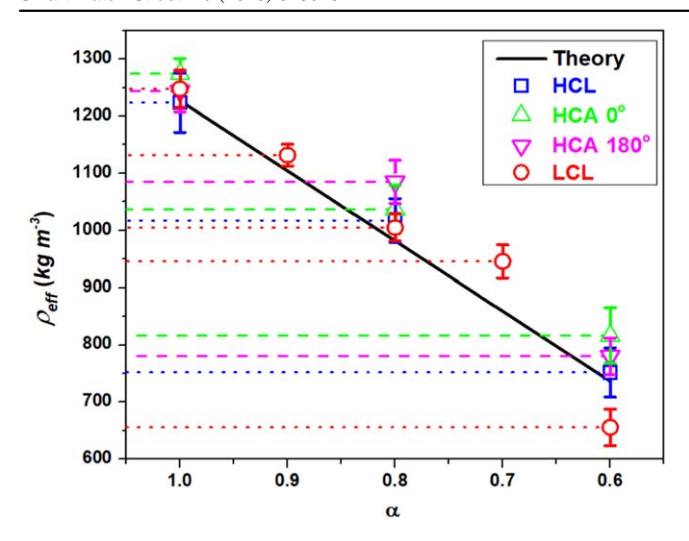


**Figure 8.** Comparsion of experimentally measured effective density and theoretical estimated density (black solid line) from  $\rho_{eff} = \rho_{ABS} r_{noz}$ ,  $_{eff} ^2 r_{noz} ^{-2}$ . The average contrast densities are obtained from the images shown in figure 4.

#### 4.3. Discussion

As figure 8 shows, both effective density imaging and characterization performed well comparing with theoretically estimated density,  $\rho_{eff} = \rho_{ABS} r_{noz, eff}^2 r_{noz}^{-2}$ . In high contrast characterization results, the calculated effective density values were about 8% higher in the 80% and 60% regions presumably due to the dissipative and dispersive effects of the ultrasonic waves in the medium. These effects are apparent in the waveform and are likely to be introduced by the porosity in the sample (figure 7). The speed of sound values in those two regions was lower than expected due to dispersion effect, which finally resulted in higher effective density values estimated from equation (2). For the zones manufactured with 100% flow rate, the estimated effective density is slightly lower than the theoretical calculation because small sizes porous still existed in printed objects in both types of experiments. The effective density imaging showed better agreement (averaged values) with theoretically calculated values in high contrast sample than lower image resolution. The imaging resolution on low contrast samples showed much higher clarity but lower accuracy in averaged values especially at 70% and 60% flow rate regions. The averaged errors in effective density measurement over all reported experiments are stated in table A1.

The effective density imaging and characterization were able to remotely measure the density distribution on FDM 3D printed objects non-destructively in terms of either rasterscanned images or single measurement as characterization. With a calibration, the effective density imaging could inspect the quality of FDM printed products in future study. Further studies can be carried out to correlate the FDM printer extruder flow rate with the health of printing tools such as the condition of the extruding motor, gear, and nozzle. The condition of the printer elements and printing quality could be monitored *in situ* by attaching an ultrasound transducer under

the printer substrate with effective density diagnostic tools. This study focused on the FDM 3D printed objects for proving the concept. But in principle, this technique could be applied on other manufacturing processes and other 3D printing techniques, such as casting, molding, and other additive manufacturing, such as stereolithography (SLA) and selective laser melting. Any manufacturing process where the porosity or density affect the quality of the manufactured products, the processing quality could be monitoring and inspecting by comparing effective density measurements to a standard calibrated reference. For increasing lateral and axis detection resolution, an acoustic lens [30] could also be involved into the inspection.

#### 5. Conclusion

In this study, the study of a novel technique of ultrasonic density evaluation technique applied on FDM 3D printed structure was reported. The printed objects with different density regions were distinguished in terms of effective density images. The technique was the first non-destructive and non-contact testing method to determine FDM 3D printing quality. The examined effective density had strong agreement with theoretically calculated values. In future study, the technique could be practically combined into FDM printing processing to achieve real time quality inspection of printing objects *in situ*.

# **Acknowledgments**

This work is supported by an Emerging Frontiers in Research and Innovation (EFRI) grant from the National Science Foundation (NSF Grant No. 1741677) and Advanced Materials and Manufacturing Processes Institute (AMMPI) 2019 SEED grants.

# **Appendix**

3D printing setting list:

Skin layer thickness: 0.35 mm. Infill layer thickness: 0.4 mm. Extruding speed: 300 mm min<sup>-1</sup>.

Wall thickness: 2 layers.

Infill pattern: Fully infilled, lines.

Extruding width: 0.4 mm.

**Table A1.** Percentage of errors between effective density imaging measured values and theoretically calculated values.

Flow rate	HCL	LCL	HCA 0°	HCA 180°
1	4.25%	2.64%	2.12%	2.89%
0.9		1.68%		
0.8	3.74%	2.39%	4.05%	3.50%
0.7		3.07%		
0.6	5.72%	4.88%	6.00%	4.10%

#### **ORCID iDs**

Yuqi Jin https://orcid.org/0000-0001-7798-8086 Hyeonu Heo https://orcid.org/0000-0003-0116-0471 Arup Neogi https://orcid.org/0000-0003-3075-8683

#### References

- [1] Heidari-Rarani M, Rafiee-Afarani M and Zahedi A M 2019 Mechanical characterization of FDM 3D printing of continuous carbon fiber reinforced PLA composites Composites B 175 107147
- [2] Wu P, Wang J and Wang X 2016 A critical review of the use of 3D printing in the construction industry *Autom. Constr.* 68 21–31
- [3] Jin Y, Rao A, Brinkman W and Choi T-Y 2017 3D printingassisted energy loss testing of artificial aortic heart valves Eng. Sci. Technol.: Int. J. (ESTIJ) 7 11–4
- [4] Ren H, Zhang H, Jin Y, Gu Y and Arigong B 2019 A novel 2D 3 × 3 Nolen matrix for 2D beamforming applications *IEEE Trans. Microw. Theory Tech.* 67 4622–31
- [5] Hawatmeh D F, LeBlanc S, Deffenbaugh P and Weller T 2016 Embedded 6 GHz 3D printed half-wave dipole antenna IEEE Antennas Wirel. Propag. Lett. 16 145–8
- [6] Wolfs R J M, Bos F P and Salet T A M 2018 Early age mechanical behaviour of 3D printed concrete: Numerical modelling and experimental testing *Cement Concr. Res.* 106 103–16
- [7] Cantrell J T et al 2017 Experimental characterization of the mechanical properties of 3D-printed ABS and polycarbonate parts Rapid Prototyping J. 23 811–24
- [8] Zou R, Xia Y, Liu S, Hu P, Hou W, Hu Q and Shan C 2016 Isotropic and anisotropic elasticity and yielding of 3D printed material *Composites* B 99 506–13
- [9] Farbman D and McCoy C 2016 Materials testing of 3D printed ABS and PLA samples to guide mechanical design ASME 2016 11th Int. Manufacturing Science and Engineering Conf. American Society of Mechanical Engineers Digital Collection (https://doi.org/10.1115/MSEC2016-8668)
- [10] Alaimo G, Marconi S, Costato L and Auricchio F Influence of meso-structure and chemical composition on FDM 3Dprinted parts Composites B 113 371–80
- [11] Moon S K, Tan Y E, Hwang J and Yoon Y-J 2014 Application of 3D printing technology for designing light-weight unmanned aerial vehicle wing structures *Int. J. Precis. Eng. Manuf.-Green Technol.* 1 223–8
- [12] Panda B P S C, Mohamed N A N, Tay Y W D and Tan M J 2018 Measurement of tensile bond strength of 3D printed geopolymer mortar *Measurement* 113 108–16
- [13] Sanjayan J G, Nematollahi B, Xia M and Marchment T 2018 Effect of surface moisture on inter-layer strength of 3D printed concrete Constr. Build. Mater. 172 468–75
- [14] El-Hajje A, Kolos E C, Wang J K, Maleksaeedi S, He Z, Wiria F E, Choong C and Ruys A J 2014 Physical and mechanical characterisation of 3D-printed porous titanium for biomedical applications J. Mater. Sci., Mater. Med. 25 2471–80

- [15] Chua C K, Wong C H and Yeong W Y 2017 Standards, quality control, and measurement sciences in 3D printing and additive manufacturing (New York: Academic)
- [16] Otten W, Pajor R, Schmidt S, Baveye P C, Hague R and Falconer R E 2012 Combining x-ray CT and 3D printing technology to produce microcosms with replicable, complex pore geometries *Soil Biol. Biochem.* 51 53–5
- [17] Miller B W, Moore J W, Barrett H H, Fryé T, Adler S, Sery J and Furenlid L R 2011 3D printing in x-ray and gamma-ray imaging: A novel method for fabricating highdensity imaging apertures *Nucl. Instrum. Methods Phys. Res.* A 659 262–8
- [18] Huber C et al 2016 3D print of polymer bonded rare-earth magnets, and 3D magnetic field scanning with an end-user 3D printer Appl. Phys. Lett. 109 162401
- [19] McSkimin H J 1964 Ultrasonic methods for measuring the mechanical properties of liquids and solids *Phys. Acoust.: Princ. Methods* 1 271–334
- [20] Wang T, Shukla S, Nene S S, Frank M, Wheeler R W and Mishra R S 2018 Towards obtaining sound butt joint between metallurgically immiscible pure Cu and stainless steel through friction stir welding *Metall. Mater. Trans.* A 49A 2578–82
- [21] Synnevag J F, Andreas A and Holm S 2007 Adaptive beamforming applied to medical ultrasound imaging *IEEE Trans. Ultrason. Ferroelectr. Freq. Control* 54 1606–16113
- [22] Ruud C O and Green R 1984 Nondestructive Methods for Material Property Determination (New York: Plenum Press) p 410
- [23] Chapelon J-Y and Blanc E 1998 Use of a-mode echography for monitoring the position of a patient during ultrasound therapy US Patent 5,720,286
- [24] Matrone G, Savoia A S, Caliano G and Magenes G 2014 The delay multiply and sum beamforming algorithm in ultrasound B-mode medical imaging *IEEE Trans. Med. Imaging* 34 940–9
- [25] Youk J H, Son E J, Park A Y and Kim J-A 2014 Shear-wave elastography for breast masses: local shear wave speed (m/ sec) versus Young modulus (kPa) *Ultrasonography* 33 34
- [26] Yoshitake Y, Takai Y, Kanehisa H and Shinohara M 2014 Muscle shear modulus measured with ultrasound shear-wave elastography across a wide range of contraction intensity *Muscle Nerve* 50 103–13
- [27] Jin Y, Walker E, Krokhin A, Heo H, Choi T-Y and Neogi A Enhanced instantaneous elastography in tissues and hard materials using bulk modulus and density determined without externally applied material deformation *IEEE Trans*. *Ultrason. Ferroelectr. Freq. Control* Early Access (https://doi.org/10.1109/TUFFC.2019.2950343)
- [28] Otten W P R, Schmidt S, Baveye P, Hague R and Falconer R 2012 Combining x-ray CT and 3D printing technology to produce microcosms with replicable, complex pore geometries Soil Biol. Biochem. 51 53–5
- [29] Rayegani F and Onwubolu G C 2014 Fused deposition modelling (FDM) process parameter prediction and optimization using group method for data handling (GMDH) and differential evolution (DE) *Int. J. Adv. Manuf. Technol.* 73 509–19
- [30] Walker E L, Reyes-Contreras D, Jin Y and Neogi A 2019 Tunable hybrid phononic crystal lens using thermo-acoustic polymers ACS Omega 4 16585–90